

**Atomic scale annealing effects on  $\text{In}_x\text{Ga}_{1-x}\text{N}_y\text{As}_{1-y}$  studied by TEM three-beam imaging**

Knut Müller,\* Marco Schowalter, and Andreas Rosenauer  
*Universität Bremen, Otto-Hahn-Allee 1, D-28359 Bremen, Germany*

Dongzhi Hu, Daniel M. Schaadt, and Michael Hetterich  
*Institut für Angewandte Physik and DFG Center for Functional Nanostructures (CFN), Karlsruhe Institute of Technology (KIT),  
 Wolfgang-Gaede Str. 1, D-76131 Karlsruhe, Germany*

Philippe Gilet  
*CEA LETI Minattec Campus, 17 Avenue des Martyrs, F-38054 Grenoble Cedex 9, France*

Oleg Rubel  
*Thunder Bay Regional Research Institute, 290 Munro Street, Thunder Bay, Canada  
 Lakehead University, 955 Oliver Road, Thunder Bay, Ontario, P7A 7T1 Canada and  
 Materials Science Center and Faculty of Physics, Philipps Universität Marburg, Hans-Meerwein-Straße, D-35032 Marburg, Germany*

Rafael Fritz and Kerstin Volz  
*Materials Science Center and Faculty of Physics, Philipps Universität Marburg, Hans-Meerwein-Straße, D-35032 Marburg, Germany*  
 (Received 17 December 2010; revised manuscript received 18 May 2011; published 18 July 2011)

A transmission electron microscopy (TEM) method for simultaneous measurement of indium and nitrogen content in InGaNAs at atomic scale is introduced, tested, and applied to investigate thermal annealing effects on structural properties. Our technique is based on the extraction of strain and chemical sensitive contrast from a single three-beam TEM lattice fringe image by subsequent decomposition into 220 and 020 two-beam fringe images, being free of nonlinear imaging artifacts. From comparison with simulated strain and 020 fringe amplitude, concentration maps and profiles are derived. For this purpose, the Bloch-wave approach is used with structure factors adapted for chemical bonding, static atomic displacements, as well as diffuse losses due to static and thermal disorder. Application to  $\text{In}_{0.28}\text{Ga}_{0.72}\text{N}_{0.025}\text{As}_{0.975}$  before and after annealing at 670 °C yields dissolution of In-rich islands and N-rich clusters and formation of a quantum well with nearly constant thickness and homogeneous elemental distributions, resulting in symmetric profiles along growth direction. To verify that these structural transitions are indeed correlated with typically observed changes of optical properties during thermal annealing, photoluminescence spectra are presented, revealing an increase in intensity by a factor of 20 and a strong blue shift of 60 meV.

DOI: [10.1103/PhysRevB.84.045316](https://doi.org/10.1103/PhysRevB.84.045316)

PACS number(s): 81.40.Tv, 68.35.Dv, 68.35.bg

**I. INTRODUCTION**

Investigation of dilute nitride semiconductor nanostructures, such as  $\text{In}_x\text{Ga}_{1-x}\text{N}_y\text{As}_{1-y}$ , has raised interest within several physical disciplines, namely semiconductor epitaxy, optics, and solid-state theory. After the first successful epitaxy of  $\text{In}_x\text{Ga}_{1-x}\text{N}_y\text{As}_{1-y}$  on GaAs by Kondow *et al.*,<sup>1</sup> it was quickly noticed that as-grown samples indeed exhibit room-temperature photoluminescence (PL) near 1.3  $\mu\text{m}$ , which is principally suitable for signal transmission in optical fibers. However, PL peaks of as-grown samples are relatively weak and broad,<sup>1-3</sup> so postgrowth thermal annealing has since been used to drastically improve PL peak intensity and width. Unfortunately, this happens at the expense of spectral performance because PL emission shifts several tens of nanometers to smaller wavelengths, depending on annealing temperature and stabilizing atmosphere.<sup>3-7</sup>

In order to explain this blue shift in the PL signal, researchers additionally focused on structural characteristics of InGaNAs before and after annealing. Subsequent measurements have then frequently been interpreted by accompanying studies of the coordination of nitrogen<sup>4,8-12</sup> and of long-range ordering of indium and nitrogen.<sup>5,13</sup> However, it is interesting

to compare the progress in epitaxy, optics, and theoretical modeling with that in the field of transmission electron microscopy (TEM), where no versatile method exists that deals with unambiguous atomic-scale mapping of both indium and nitrogen content. The method developed by Grillo *et al.*<sup>14</sup> is based on a supplementary superposition of an off-zone dark field and a zone axis high-resolution TEM micrograph, making imaging of the same specimen area with atomic accuracy difficult. In a previous study that was focused on theoretical models for  $\text{In}_x\text{Ga}_{1-x}\text{N}_y\text{As}_{1-y}$  scattering factors, Müller *et al.*<sup>15</sup> used a single lattice fringe image formed by beams 000 and 020 to determine both local strain and chemically sensitive contrast simultaneously. Unfortunately, the 020 fringes vanish for certain concentrations, making strain evaluation for such specimens impossible. Concerning electron-energy loss spectroscopy, both the broad shape of the indium edge and the low nitrogen content complicate reliable elemental mapping. Similarly, the nitrogen signal in energy-dispersive x-ray spectroscopy is too low for scanning TEM mapping at the atomic scale.

In this article, we first present a three-beam method for atomic-scale measurement of both  $x$  and  $y$ , being suitable for

structural characterization of quaternary zinc-blende alloys in view of the aspects mentioned at the beginning. Both compositions are extracted from a single TEM lattice fringe image based on the interference of 000, 220, and 020. Since the 220 reflection is very intense for all compositions, the 220 lattice fringes are used to measure strain throughout the whole TEM image. Additionally, the chemically sensitive signal is extracted from the 020 lattice fringes. Thus, our technique provides strain and chemically sensitive contrast simultaneously for each lattice point, even if the 020 structure factor is zero. Regarding three-beam imaging, a special objective aperture has been fabricated to eliminate nonlinear contributions to the respective diffractogram reflections. After summary of experimental items in Sec. II, a detailed description of the method will be given in Sec. III.

As most quantitative methods, our technique requires comparison with simulated reference intensities. Thus, a prerequisite for the Bloch-wave simulations used here is an adequate model for InGaAs scattering factors under the influence of static atomic displacements (SAD) and bonding. In principal, this was reported in a previous study,<sup>15</sup> where SAD were derived using valence force field (VFF) methods<sup>16</sup> and joined with an atomistic approach for chemical bonding in terms of modified atomic scattering amplitudes (MASA).<sup>17</sup> However, SAD include diffuse scattered electrons adding to the thermal background in a diffraction pattern or, equivalently, lacking in Bragg scattered beams. Besides optimized imaging conditions and the reference data itself, a theoretical study of appropriate absorptive form factors will be given in Sec. IV A via comparison of Bloch-wave pendellösung plots with a full multislice result.

Second, we apply our three-beam method to investigate thermal annealing effects on structural properties of an  $\text{In}_{0.28}\text{Ga}_{0.72}\text{N}_{0.025}\text{As}_{0.975}$  layer in Sec. V. Photoluminescence spectra before and after thermal annealing show a blue shift of 65 nm, which is interpreted by means of the three-beam results. As to the TEM results, we give errors stemming from inaccurately known specimen thickness and verify the reliability of our method by application to a well-characterized  $\text{In}_{0.08}\text{Ga}_{0.92}\text{N}_{0.03}\text{As}_{0.97}$  solar cell structure. Finally, methodical and physical results will be discussed in Sec. VI, before main conclusions will be summarized in Sec. VII.

## II. EXPERIMENTAL DETAILS

A 7-nm-thick quantum well with nominal composition  $\text{In}_{0.28}\text{Ga}_{0.72}\text{N}_{0.025}\text{As}_{0.975}$ , being a typical setup for InGaAs laser structures, was grown by molecular beam epitaxy (MBE) and is referred to as sample I in the following. Part of this sample was treated by thermal annealing at 670° C for 15 min in a  $\text{N}_2$  atmosphere. When dealing with comparison of the annealed and as-grown part, we refer to the former as sample Ia and to the latter as sample Ib.

A 15-nm-thick lattice-matched quantum well with nominal composition  $\text{In}_{0.08}\text{Ga}_{0.92}\text{N}_{0.03}\text{As}_{0.97}$ , being a typical setup for InGaAs solar cell structures, was grown by metal organic vapor phase epitaxy (MOVPE). We refer to this as sample II whose composition has been studied before<sup>15</sup> and which therefore helps to verify the three-beam approach for composition mapping presented here.

Cross-sectional TEM specimens have been prepared conventionally in zone axis [001] by first mechanical grinding and second argon ion polishing using a Gatan precision ion polishing system operating at angles of  $\pm 3^\circ$ – $5^\circ$  and an energy of 3.5 keV. An FEI Titan 80/300 TEM facility equipped with a corrector for the spherical aberration of the objective lens, operated at 300 kV, was used for all TEM measurements. All images have been recorded on a  $2K \times 2K$  charge-coupled device camera. An L-shaped objective aperture consisting of two  $12.5 \times 25 \mu\text{m}$  rectangles oriented by  $90^\circ$  was etched into a  $7\text{-}\mu\text{m}$ -thick platinum foil using an FEI Nova 200 NanoLab focused ion beam facility.

The room-temperature near-infrared PL spectra of samples Ia and Ib have been dispersed using a 46-cm monochromator equipped with a 600 lines/mm grating and detected by a thermoelectrically cooled InGaAs detector using a lock-in technique. A laser diode emitting at a wavelength of 670 nm with a power of about 200 mW was used for excitation.

## III. DESCRIPTION OF THE METHOD

In high-resolution TEM, inclusion of more than two diffracted beams in the imaging process principally involves nonlinear contributions to phases and amplitudes of diffractogram reflections. It is thus necessary to constrain the number of diffracted beams as far as possible with respect to quantities that are to be extracted from the image. In order to measure strain from 220 and chemically sensitive contrast from 020 lattice fringes, an objective aperture is preferable that transmits the beams  $\vec{g}_1 = (000)$ ,  $\vec{g}_2 = (020)$ , and  $\vec{g}_3 = (220)$ . In the frame of nonlinear imaging theory, the image intensity at position  $\vec{r}$  reads

$$I(\vec{r}) = A_1^2 + A_2^2 + A_3^2 + 2A_1A_2T_{12} \cos(2\pi\vec{g}_2\vec{r} - \phi_{12} - \varphi_{12}) + 2A_1A_3T_{13} \cos(2\pi\vec{g}_3\vec{r} - \phi_{13} - \varphi_{13}) + 2A_2A_3T_{23} \cos[2\pi(\vec{g}_2 - \vec{g}_3)\vec{r} + \phi_{23} + \varphi_{23}]. \quad (1)$$

In Eq. (1),  $A_n \exp(i\varphi_n)$  is the amplitude of diffracted beam  $n$ ,  $\varphi_{nm} = \varphi_n - \varphi_m$  is the phase difference between beams  $n, m$ , and  $T_{nm} \exp(i\phi_{nm})$  is the corresponding transmission cross coefficient. The first two cosine terms in Eq. (1) express conventional two-beam images, i.e., interference of one diffracted with the primary beam. The last summand, however, originates from nonlinear imaging and causes additional diffractogram reflections at  $\pm(200)$ . Thus, 020 and 220 fringes are not affected by nonlinear imaging, so the three-beam image can be decomposed into conventional two beam fringe images by Fourier filtering.

Figure 1(a) depicts an experimental noise-filtered three-beam image containing an interface between  $\text{In}_x\text{Ga}_{1-x}\text{N}_y\text{As}_{1-y}$  and GaAs in the center. The superposition of 020 and 220 fringes is clearly visible in both image and diffractogram bottom left. However, the latter depicts also weak  $\pm(200)$  reflections, although only beams (000), (020), and (220) were selected by our L-shaped objective aperture. The advantage to include the (220) beam becomes obvious in Figs. 1(b)–1(d): At certain concentrations  $(x, y)$ , the 020 structure factor becomes zero and changes sign, resulting in nearly vanishing 020 fringes and a phase shift of half a period

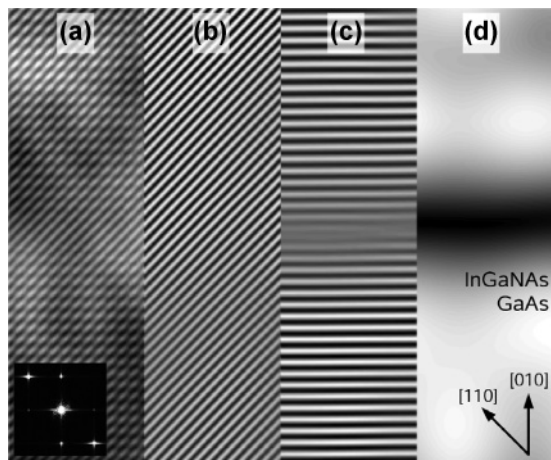


FIG. 1. Decomposition of an experimental three-beam image (a) acquired near zone axis [001] with a Laue circle center at (4.2 0 0). Via Fourier filtering, 220 and 020 fringe images (b) and (c) are obtained by keeping the primary beam and a circular area around the respective reflection in the diffractogram shown as an inset in (a). The lower half of the image corresponds to pure GaAs, evolving to an  $\text{In}_{0.28}\text{Ga}_{0.72}\text{N}_{0.025}\text{As}_{0.975}$  quantum well in the upper half. The chemically sensitive 020 fringe amplitude obtained by keeping only frequencies close to the 020 reflection in the diffractogram and inverse Fourier transformation is shown in part (d). Contrast has been adjusted for better visibility.

as depicted in Figs. 1(c) and 1(d). In contrast, the amplitude of the 220 fringes in Fig. 1(b) is nearly constant throughout the interface, allowing for strain measurement in the whole region.

The term *strain* requires some attention since it refers to the distortion of a bulk InGaNaNs cell in terms of the relaxed cell dimensions. In practice, we apply elasticity theory to calculate the lattice parameter in growth direction as a function of composition and normalize the result to the lattice parameter of the GaAs substrate. As growth is along [010] here, the 020 fringe distance can be used to access this relative lattice parameter, which is denoted by  $\varepsilon_{[010]}$  in the following. However,  $45^\circ$  rotation of the 220 fringes with respect to growth direction [010] induces a conversion factor

$$\varepsilon_{[010]} = \frac{\varepsilon_{[110]}}{\sqrt{2 - \varepsilon_{[110]}^2}} \quad (2)$$

in order to calculate  $\varepsilon_{[010]}$  in growth direction from the measured quantity  $\varepsilon_{[110]}$ . Equation (2) requires precise measurement of the local fringe distances, because small errors for  $\varepsilon_{[110]}$  translate to considerably larger errors for  $\varepsilon_{[010]}$ . For example, a fluctuation of  $\Delta\varepsilon_{[110]} = 0.01$  yields  $\Delta\varepsilon_{[010]} = 0.02$ . In practice, we apply a Wiener noise filter to the 220 fringe image and detect preliminary maxima positions by searching for pixels with highest intensity on each fringe. After that, local cosines are fitted at each maximum, yielding positions with subpixel accuracy. Then,  $\varepsilon_{[010]}$  is obtained by application of Eq. (2) to local distances along [110] between adjacent maxima, normalized to the mean distance in a GaAs reference region. Note that a cosine is the exact representation of the image intensity according to Eq. (1).

Concerning evaluation of 020 fringe amplitude, we proceed as follows<sup>15,18</sup>: In the diffractogram, we isolate the 020

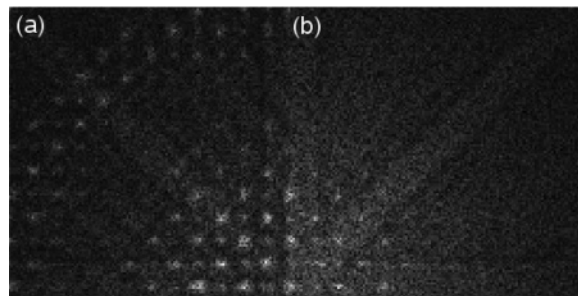


FIG. 2. Two quarters of a  $\text{GaN}_{0.06}\text{As}_{0.94}$  diffraction pattern in an exact [001] zone axis orientation for 300-kV electrons, simulated<sup>19</sup> with the multislice approach in the frozen lattice approximation. In quarter (a), the diffuse background stems from SAD only, whereas both SAD and thermal displacements according to 300 K from Schowalter *et al.*<sup>20</sup> are applied for part (b).

reflection and obtain the local 020 fringe amplitude. Regions of known composition, usually GaAs buffer layers, are used for a two-dimensional polynomial surface fit, yielding the expected signal for pure GaAs throughout the whole image, to which the 020 fringe amplitude is normalized. This normalized 020 amplitude  $a_N$ , defined by

$$a_N(\vec{r}, \vec{c}, t, x, y) = \frac{A_1(\vec{r}, \vec{c}, t, x, y)A_2(\vec{r}, \vec{c}, t, x, y)}{A_1(\vec{r}, \vec{c}, t, 0, 0)A_2(\vec{r}, \vec{c}, t, 0, 0)}, \quad (3)$$

in general depends not only on compositions  $x$  and  $y$  at position  $\vec{r}$  (chemical sensitivity) but also on specimen thickness  $t$  and specimen orientation  $\vec{c}$ , measured in terms of the position of the Laue circle center. Since the specimen thickness is usually inaccurately known, Sec. IV B deals with the derivation of orientations  $\vec{c}$  being robust against this error.

Finally, each point  $\vec{r}$  in the image can be assigned a concentration pair  $(x, y)$  by comparison of  $\varepsilon_{[010]}$  and  $a_N(\vec{r}, \vec{c}, t, x, y)$  with their simulated counterparts. Whereas concentration-dependent strain reference data can be calculated using Vegard's rule in combination with elasticity theory, care must be taken for the simulation of  $a_N$  because the method relies on significant presence of both the 020 and the 220 beam that can only be achieved by small specimen tilts. This in turn causes strong dynamical effects on the beam amplitudes and phases in Eq. (1), which will be analyzed in the following.

## IV. SIMULATION OF REFERENCE INTENSITIES

### A. Treatment of disorder in the Bloch-wave approach

The oversimplified model of an ideal crystal, on which the Bloch theorem and the expansion of the crystal potential in Fourier series rely, has experienced numerous modifications in the past regarding simulation of correct Bragg beam amplitudes even in the presence of disorder: Thermal disorder not only leads to Debye-Waller damping of atomic scattering amplitudes but also causes an imaginary (absorptive) part (e.g., Ref. 21), for which absorptive form factors have been published in, e.g., Refs. 22 and 23 Static atomic displacements have been shown to significantly alter the nonabsorptive part of the crystal potential.<sup>15,24,25</sup> Besides this direct influence on structure factors, Fig. 2(a) illustrates that SAD lead to an increase of the diffuse background in a diffraction pattern and

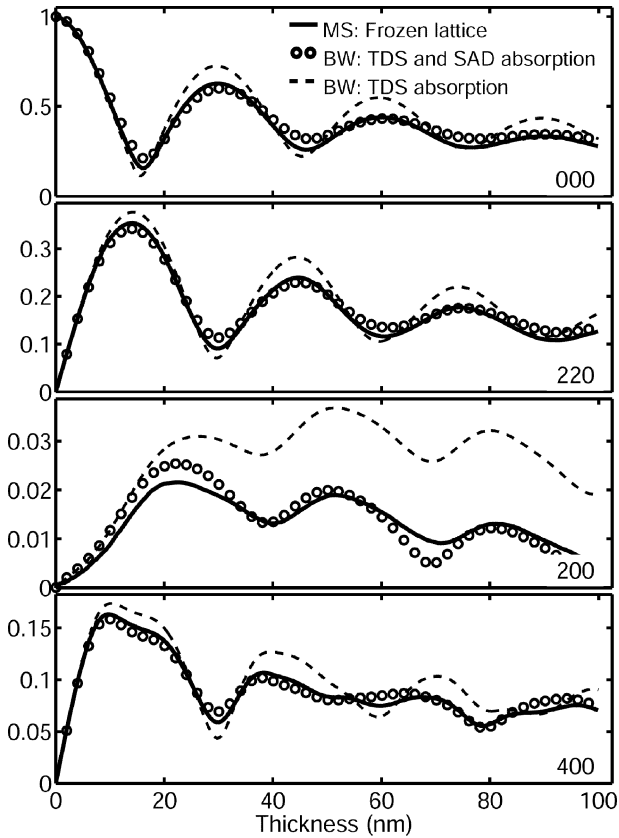


FIG. 3. Pendellösung plots of diffracted beam amplitudes for a strain relaxed  $\text{In}_{0.25}\text{Ga}_{0.75}\text{N}_{0.05}\text{As}_{0.95}$  cell using multislice (MS) and Bloch-wave (BW) methods for 300-kV electrons incident exactly along [001] zone axis. The MS graphs were obtained from 10 thermal displacement configurations and by mapping the amplitude in the pixels that correspond to the respective Bragg beam. Atomic scattering amplitudes were taken from Weickenmeier and Kohl<sup>22</sup> in all three cases. The BW simulations contain absorptive form factors due to thermal (dashed curve), as well as both thermal and static (circles) disorders, respectively.

must thus be included in the absorptive part of the crystal potential, too. In contrast to thermal diffuse scattering (TDS), which was additionally accounted for in Fig. 2(b), these electrons remain in the vicinity of Bragg peaks. Here, the simulation was performed with the STEMSIM<sup>19</sup> software using the multislice method and the frozen lattice approximation applied to  $\text{GaN}_{0.06}\text{As}_{0.94}$ . Static atomic displacements were derived with VFF.<sup>16,24</sup>

In Fig. 3, we present a study of thickness dependencies for selected Bragg beam amplitudes in a 100-nm-thick  $10 \times 10$   $\text{In}_{0.25}\text{Ga}_{0.75}\text{N}_{0.05}\text{As}_{0.95}$  supercell. Electron beam incidence was exactly along [001] zone axis and SAD have been obtained by VFF. The solid curves correspond to the frozen lattice multislice result, averaged over 10 thermal displacement configurations, and are regarded as the most reliable ones because they contain both the dynamics of diffuse and Bragg scattered electrons.<sup>26</sup> The dashed curves originate from Bloch-wave simulations with conventional absorptive form factors according to the Debye parameters used in the multislice simulation, too. Comparison with the solid curves reveals

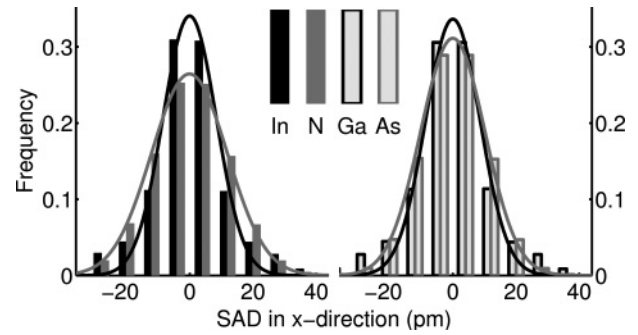


FIG. 4. Histograms of SAD in the  $x$  direction for individual atomic species in a strain relaxed 100-nm-thick  $10 \times 10$   $\text{In}_{0.25}\text{Ga}_{0.75}\text{N}_{0.05}\text{As}_{0.95}$  supercell (bars) with respective Gaussian least-squares fits (solid lines). Mean displacements are derived from the standard deviations in the  $x$ ,  $y$ , and  $z$  directions and serve for the calculation of absorptive form factors analogous to those for mean thermal displacements from Ref. 22.

differences that become most significant for the 200 reflection, where absorption is clearly underestimated.

Physically, atom size effects introduced by a foreign atom on the gallium or arsenic sublattice, can be regarded as a point defect. The application of Huang scattering theory<sup>27</sup> then yields expressions that are formally equivalent with the treatment of TDS if SAD show a Gaussian distribution.<sup>28,29</sup> Therefore, a comfortable way to include Huang scattering losses in the absorptive potential would be to calculate absorptive form factors for each atomic species as conventionally defined for TDS losses<sup>22</sup> based on the width of the distribution of SAD for this species, provided that SAD satisfy a Gaussian distribution.

For a strain relaxed  $\text{In}_{0.25}\text{Ga}_{0.75}\text{N}_{0.05}\text{As}_{0.95}$  cell consisting of approximately 141 000 atoms, Fig. 4 shows histograms of the displacements in the  $x$  direction for each of the four constituents and corresponding least-squares Gaussian fits. The latter is in nearly perfect agreement with SAD of nitrogen and arsenic, respectively. For indium and gallium, the Gaussian slightly underestimates large displacements originating from strong local strains in the immediate vicinity of nitrogen atoms. However, the principal similarity between fit and histogram motivates the calculation of absorptive form factors from Weickenmeier and Kohl<sup>22</sup> according to standard deviation of the respective SAD distribution. Total diffuse losses are then incorporated in the potentials for the Bloch-wave simulations as an effective absorptive form factor for each atom, being the sum of TDS and SAD contributions.

Thickness dependencies derived this way are depicted as circles in Fig. 3 and exhibit an improved accordance with the multislice result. Nevertheless, the agreement is not perfect, which can be explained by the fact that Huang scattering occurs at definite positions in the crystal where SAD are large. This is translated to a continuous, mean absorption in the Bloch-wave approach, so we expect mainly the damping envelopes to be well represented, as can be verified best for the 200 beam. Moreover, histograms in Fig. 4 are not exactly Gaussian.

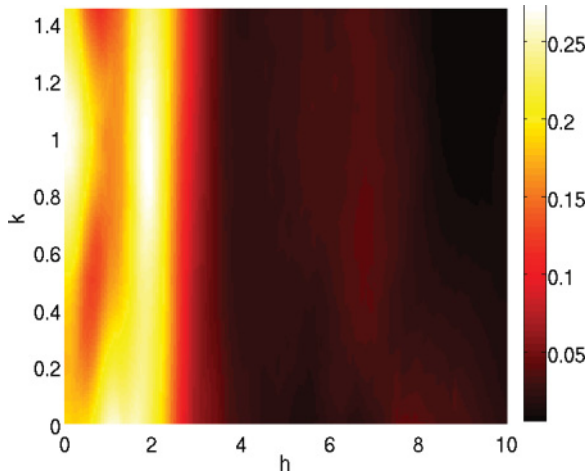


FIG. 5. (Color online) On the thickness dependence of  $a_N(\vec{c} = (h k 0), t, x = 0.08, y = 0.03)$  as a function of specimen tilt. The standard deviation  $\sigma_t(h, k)$  derived from thickness characteristics of  $a_N(t)$  was normalized to  $a_N(1 \text{ nm})$  and is depicted color-coded, showing that tilts with  $h > 3$  significantly minimize dependence on thickness.

### B. Specimen tilt

In contrast to systematic-row-like imaging conditions used for dark-field or two-beam interference patterns,<sup>14,15,18</sup> inclusion of the 220 reflection pushes incidence further toward zone axis [001]. As this leads to an excitation of more diffracted beams and hence more complex dynamics among them, the amplitude  $a_N$  in Eq. (3) may exhibit stronger thickness dependence than in the systematic row case. In order to study this dependence with respect to specimen tilt, we exemplarily calculated  $a_N(t)$  for a VFF-relaxed  $\text{In}_{0.08}\text{Ga}_{0.92}\text{N}_{0.03}\text{As}_{0.97}$  structure for a series of Laue circle centers  $\vec{c}$  in a thickness range  $t \in [0 \dots 100 \text{ nm}]$ . In practice, the beam is usually focused slightly to concentrate illumination on the specimen area of interest. This was accounted for by averaging  $a_N$  over several incidences according to a beam convergence of 1.5 mrad, which was measured from the reflection disk size in a diffraction pattern. To present results in a compact manner, the standard deviation  $\sigma_t(\vec{c})$  of the thickness dependence  $a_N(t)$  was calculated for each orientation  $\vec{c} = (h k 0)$ . In order to study the relevance of  $\sigma_t(\vec{c})$  in view of the magnitude of  $a_N$  itself, it was divided by the respective normalized amplitude at a thickness of 1 nm, which, in principle, represents  $a_N$  in a kinematic approximation. The function  $\sigma_t(\vec{c})/a_N(1 \text{ nm})$  is mapped in reciprocal space in dependence on  $h$  and  $k$  in Fig. 5.

As expected, orientations close to the zone axis in the left quarter of Fig. 5 exhibit comparably strong thickness dependence with  $\sigma_t(\vec{c})/a_N(1 \text{ nm}) \in [0.1 \dots 0.25]$ . This means that the uncertainty of  $a_N$  due to unknown specimen thickness is up to 25% of the signal itself. Toward  $h \approx 3$ , the ratio  $\sigma_t(\vec{c})/a_N(1 \text{ nm})$  rapidly drops below 0.05, which is due to the fact that the  $\pm(400)$  reflections become very weak due to an increasing distance to the Ewald sphere. For  $h > 3$ ,  $\sigma_t(\vec{c})/a_N(1 \text{ nm})$  first passes a minimum around  $h \approx 5$  and then slightly increases again toward  $h = 10$ . Furthermore, the thickness dependence is rather independent of tilt  $k$  for

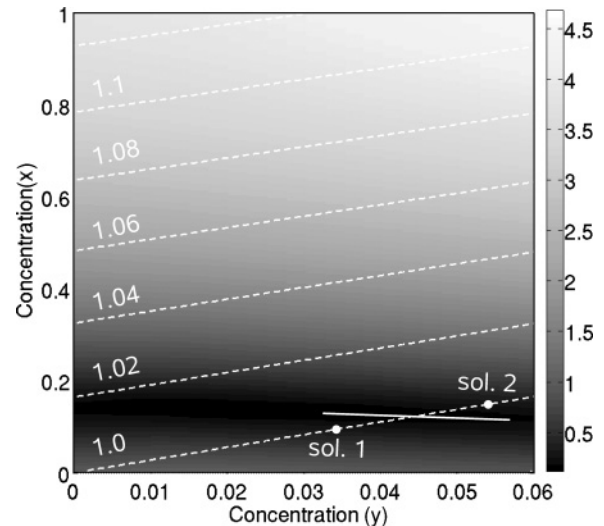


FIG. 6. Reference values for  $\varepsilon_{[010]}$  (dashed white isolines) and normalized 020 fringe amplitude  $a_N$  as a function of indium concentration  $x$  and nitrogen concentration  $y$  for a Laue circle center  $\vec{c} = (4.200)$  and for a thickness of 30 nm. Bonding and SAD are accounted for as proposed by Müller *et al.*,<sup>15</sup> except for the additional absorptive form factor due to SAD diffuse losses dealt with in Sec. IV A.

$h > 3$ , so the error due to a slight misorientation in experiment is low. In order to achieve significant 220 fringes and a passably small thickness dependence of  $a_N(t)$ , a Laue circle center  $\vec{c} = (4.200)$  was set in all three-beam experiments and simulations of reference amplitudes according to Eq. (3). Here, the uncertainty of  $a_N$  due to unknown specimen thickness is only around 2% of  $a_N$  itself.

In general, it is, of course, not only necessary to additionally study  $\sigma_t(\vec{c})$  as a function of composition but also to translate the error due to inaccurately known specimen thickness to absolute errors for the concentrations  $x$  and  $y$ . For reasons of brevity, we alternatively address this issue in Sec. V where experimental profiles are presented by giving composition ranges for the indium- and nitrogen content resulting from different assumptions for the specimen thickness.

### C. Example reference data

Figure 6 depicts  $a_N$  obtained from Bloch-wave simulations for a thickness of 30 nm exemplarily as a gray-scale map, together with reference values for the lattice parameter in growth direction, normalized to that of GaAs, as dashed isolines. Note that, except for the tilt setting and the fact that absorption due to Huang scattering was taken into account here, the reference data in Fig. 6 appear completely analogous to a former work,<sup>15</sup> to which the reader is referred to for details on bonding, VFF relaxation, and strain reference data. Another important difference is the magnitude of the normalized amplitude here, being nearly twice as large in the maximum, compared to using a Laue circle center of  $\vec{c} = (20 \ 1.5 \ 0)$ .<sup>15</sup>

Finally, each point in a three-beam image as depicted in Fig. 1 can be assigned an amplitude-strain pair that corresponds to, at most, two indium-nitrogen composition pairs separated by the dark valley in Fig. 6 as indicated by the solid white line.

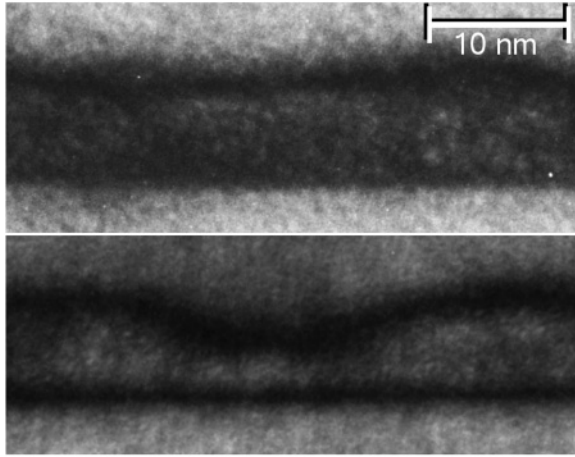


FIG. 7. The 020 dark-field overview images of samples Ia (annealed, top) and Ib (as-grown, bottom) that qualitatively show the effect of thermal annealing on layer morphology that roughly follows the null of the 020 structure factor. Both images were taken off-zone with a Laue circle center at (20 1 0).

Nevertheless, this ambiguity is not critical since both solutions (denoted by sol. 1 and sol. 2 in Fig. 6) can be well separated in experiment, as Fig. 1(d) shows.

## V. RESULTS

### A. Annealing of InGaNaNs: Structural properties

To get an impression of annealing effects on structural changes of an InGaNaNs layer, Fig. 7 contains 020 TEM dark-field images of samples Ia (annealed, top) and Ib (as-grown, bottom). To enhance visibility of the InGaNaNs layer, a systematic row condition with 020 in Bragg excitation was used here. Before annealing, we observe clear evidence for island formation on a wetting layer. After annealing, homogenization of layer thickness is found. A more quantitative result for the local indium and nitrogen distributions will now be derived using our three-beam method. In the following, optimized imaging conditions derived in Sec. IV B with a Laue circle center at (4.2 0 0) were used.

Before turning toward the elemental distributions, we exemplify the evaluation of normalized fringe distance  $\varepsilon_{[010]}$  and contrast using sample Ia. Parts of the local distance and amplitude maps, having been derived from a TEM three-beam image as explained in Sec. III, are depicted in Fig. 8. Each pixel on the left corresponds to one local result for  $\varepsilon_{[010]}$ , clearly exhibiting GaAs buffer layers with  $\varepsilon_{[010]} \approx 1.0$  and a strained InGaNaNs layer with a thickness of about 10 nm with  $\varepsilon_{[010]} \approx 1.025$  in the maximum. The right-hand side of Fig. 8 shows the normalized amplitude  $a_N$  for the same specimen region. Here, two different regimes appear according to indium contents below and above the intensity valley in Fig. 6. Note that precise data for  $\varepsilon_{[010]}$  are available also where  $a_N$  nearly vanishes.

Comparison with reference data as described in Sec. IV C for thicknesses between 10 and 80 nm and subdivision of the TEM image in high- and low-indium sections yields local distributions of indium and nitrogen that are shown in Figs. 9(a) and 9(b) exemplarily for a thickness of 30 nm. To

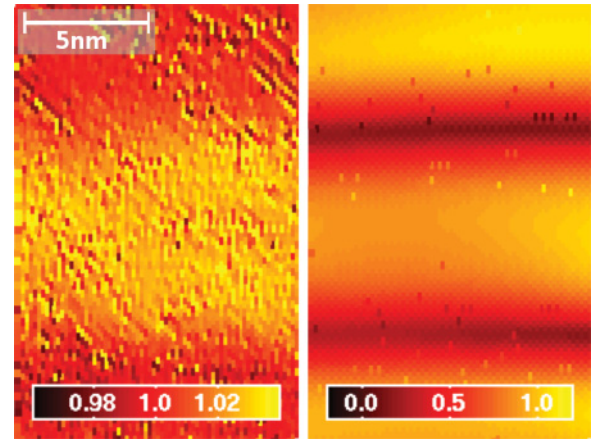


FIG. 8. (Color online) Experimental maps for the local fringe distance (normalized to GaAs)  $\varepsilon_{[010]}$  (left) and chemically sensitive fringe amplitude  $a_N$  (right) for sample Ia. Both maps have been extracted from the same three-beam TEM image by evaluation of local 220 fringe distances and Eq. (2) and 020 fringe amplitude. The Laue circle center was set at (4.2 0 0).

allow for composition fluctuations around zero in the GaAs buffer layers due to statistical errors in measurements of local fringe distances and normalized amplitudes, we extrapolated our reference data down to concentrations of  $-0.05$ . Both maps in Fig. 9 reveal a more or less homogeneous layer thickness and stoichiometry in a lateral direction with  $x \in [0 \dots 0.28]$  and  $y \in [0 \dots 0.03]$ , respectively. However, a slight indium enrichment of 0.03 appears at the left and right edges of Fig. 9(a).

The lateral homogeneity motivates an analysis of characteristic features on the basis of concentration profiles presented in Fig. 9(c), which originate from lateral averages over the full widths in Figs. 9(a) (dashed line) and 9(b) (solid line), respectively. For indium, a symmetric, Gaussian-shaped profile is observed with a maximum of  $x = 0.27$ . In contrast, the nitrogen profile is shifted by about 2 nm in the growth direction, leading to slight enrichment up to  $y = 0.03$  in the upper half of the quantum well.

Furthermore, Fig. 9(c) contains two types of error displayed in the form of error bars and a gray corridor, respectively. The former corresponds to the standard deviation derived from lateral averages in the two-dimensional elemental maps [Figs. 9(a) and 9(b)]. For better visibility, this error is drawn only every 2 nm. The latter error results from elemental maps for which different specimen thicknesses were assumed. In this respect, the gray area indicates the concentration range derived from profiles corresponding to specimen thicknesses between 10 and 80 nm in steps of 5 nm and is thus a direct measure of the error induced by inaccurately known specimen thickness. Whereas the statistical error (black bars) takes nearly constant values of  $\pm 0.01$  and is widely independent on  $x, y$  and the atomic species, the imprecision due to unknown specimen thickness mostly affects the indium measurement and significantly depends on the magnitude of  $x$ , resulting in a maximum absolute error of  $\pm 0.01$  in the quantum well center.

As to structural changes during annealing it is instructive to compare sample Ia with its as-grown counterpart Ib whose composition maps are depicted in Figs. 10(a) and

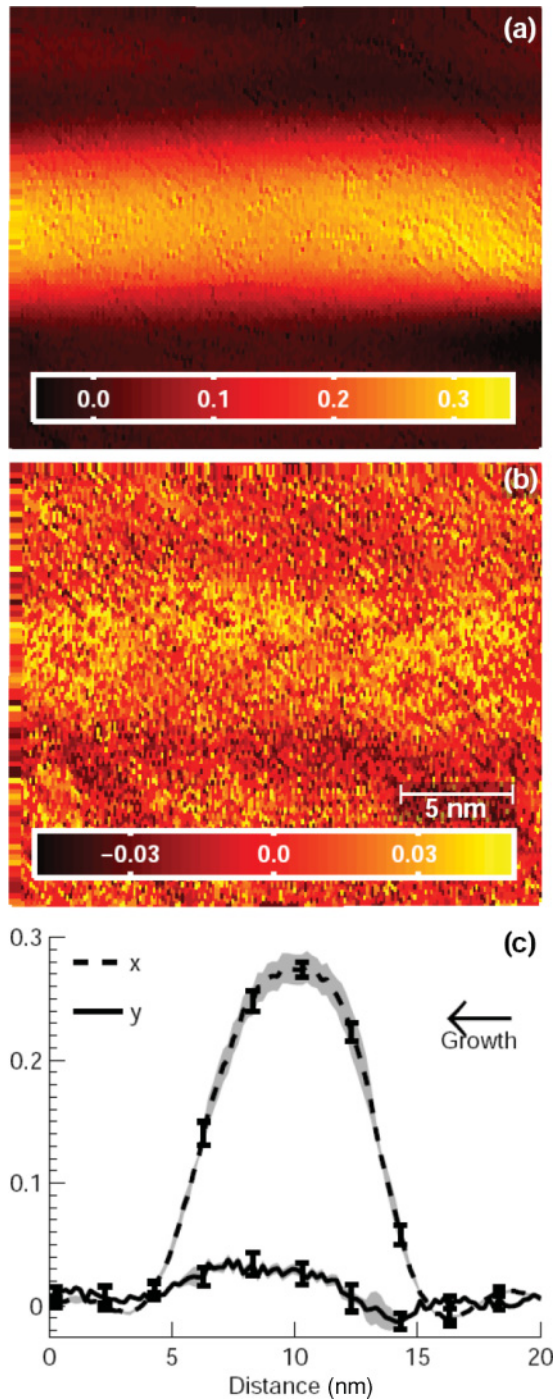


FIG. 9. (Color online) (a) Local indium- and (b) local nitrogen concentration for sample Ia. (c) Profiles obtained by averaging horizontally in (a) and (b). Error bars indicate statistical fluctuations, and the gray corridor is a measure of error due to inaccurate knowledge of the specimen thickness. Three-beam images had been taken in zone axis [001] with the Laue circle center at (4.2 0 0).

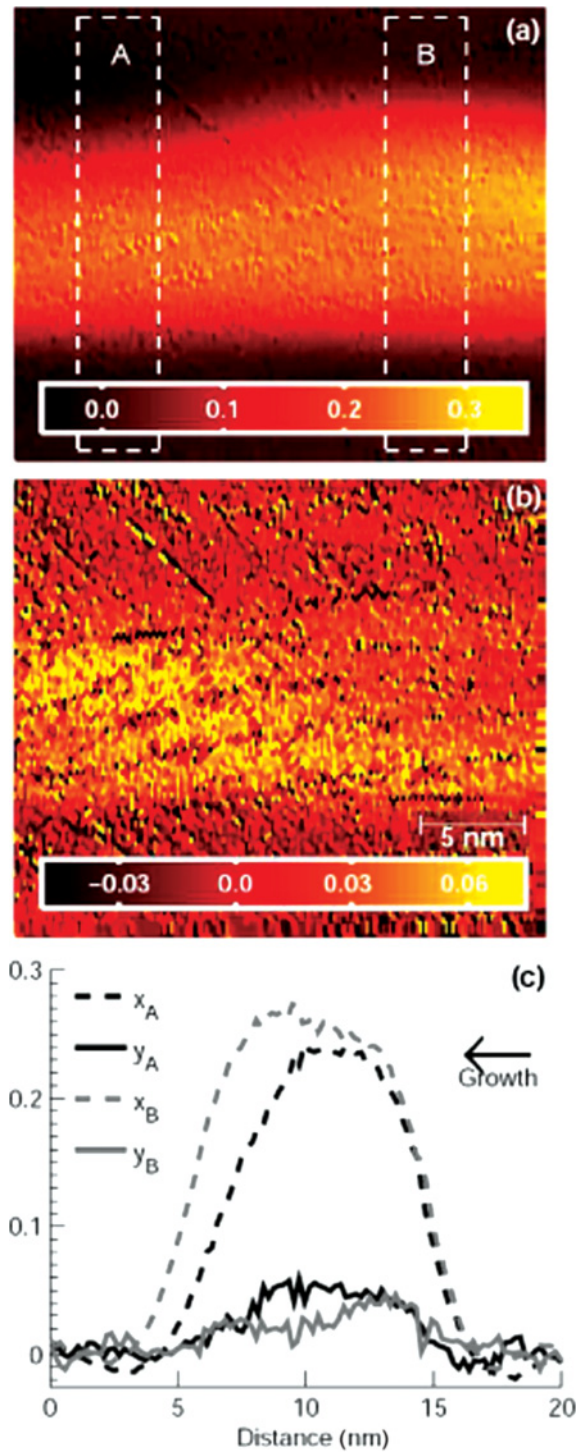


FIG. 10. (Color online) (a) Local indium- and (b) local nitrogen concentration for sample Ib. (c) Profiles obtained by averaging horizontally in the regions indicated in (a). Three-beam images had been taken in zone axis [001] with the Laue circle center at (4.2 0 0).

10(b). Regarding the indium distribution in Fig. 10(a), lateral fluctuations become evident, especially toward the upper third of the layer. Besides this morphologic separation into wetting layer and island regions, a slight indium enrichment of 0.03–0.05 appears inside the island. In contrast, the nitrogen distribution in Fig. 10(b), follows an opposite trend: Being

inhomogeneous as well, nitrogen preferably occupies the region outside the island with concentrations up to  $y \approx 0.06$ , dropping to  $y \approx 0.02$  inside the island.

Because of the inhomogeneity of the InGaNAS layer, Fig. 10(c) shows two pairs of profiles A and B, having been derived from lateral averages in the respective regions labeled

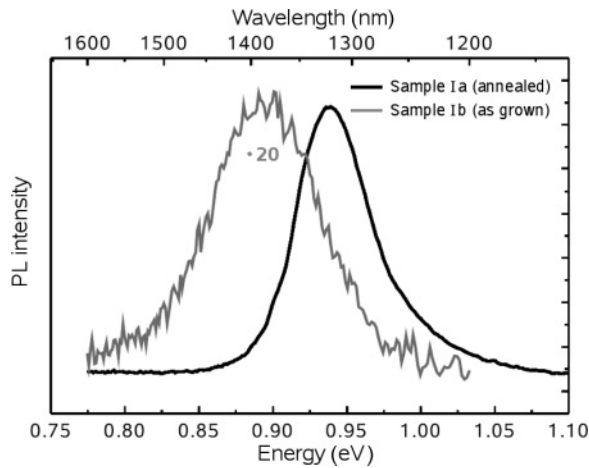


FIG. 11. Photoluminescence spectra for the laser structures investigated by TEM. After 15 min of thermal annealing under  $N_2$  stabilization, the PL peak intensity increases by a factor of 20 but shifts about 65 nm toward higher energies. Spectra were recorded at room temperature.

in Fig. 9(a). Here, error bars have been omitted to point out profile shape. However, thickness errors are comparable to those in Fig. 9(c), whereas statistical fluctuations are slightly larger due to the narrow areas for averaging. As expected, indium profiles  $x_{A,B}$  exhibit fluctuations of about 2.5 nm for the layer thickness and differ in maximum indium amounts by about 0.04. Compared to the symmetric indium profile for sample Ia, mainly the profile for  $x_A$  here is asymmetric: After gradual increase, the indium content saturates to a maximum in the upper half of the layer and then decreases rapidly.

The nitrogen profiles  $y_{A,B}$  in Fig. 10(c) differ significantly in shape and reveal different nitrogen contents as mentioned above. However,  $y_A$  shows up a maximum amount of about 0.05 and is not only symmetric with respect to the center of the wetting layer but also in phase with profile  $x_A$ . Concerning the gray curve  $y_B$ , slight nitrogen enrichment up to  $y_B = 0.05$  at incipient layer formation is observed which decays to about 0.02 during further growth and increasing indium content as expressed by profile  $x_B$ .

## B. Annealing of InGaNaS: Optical properties

As one expects from the TEM results, optical performance of samples Ia and Ib changes drastically by annealing as becomes obvious in the PL spectra shown in Fig. 11. Scaling of both curves to comparable peak intensities requires a factor of 20 for as-grown sample Ib, demonstrating strong improvement in light output efficiency by thermal annealing. Unfortunately, this happens at the expense of spectral performance as a strong blue shift of about 65 nm or, equivalantly, 60 meV occurs.

## C. Application to a solar cell structure

As a third evaluation, we present results for a lattice-matched InGaNaS layer in sample II, being a typical setup for solar cell applications. These results are of particular interest from the methodological point of view, because consistency with compositional analysis of this sample using different TEM methods<sup>15</sup> or x-ray diffraction and band-gap measurements<sup>3</sup> for a sample grown under same conditions may be checked.

Except for the fact that compositions uniquely range in the low-indium regime according to Fig. 6, evaluation is completely analogous here and results in composition maps depicted in Figs. 12(a) and 12(b). Both indium and nitrogen reveal laterally homogeneous distributions of  $x \approx 0.085$  and  $y \approx 0.03$ , respectively. As in Sec. V A, composition evaluation was performed for thicknesses between 10 and 80 nm, of which the 30 nm result is shown. A compact presentation of mean concentration characteristics and errors is shown in form of profiles in Fig. 12(c) that have been obtained from horizontal averages over the full maps [Figs. 12(a) and 12(b)]. Lateral compositional fluctuations, measured in terms of the standard deviation represented by the black bars, stay below  $\pm 0.01$  and are independent of the magnitude of  $x$  and  $y$ . In contrast, the gray corridor, in which all results between thicknesses of 10 and 80 nm fall, widens to diameters of  $\Delta x \approx 0.012$  with increasing composition. However, a mean indium composition  $\bar{x} = 0.088 \pm 0.01$  and a mean nitrogen content  $\bar{y} = 0.03 \pm 0.01$  can be assigned to sample II from Fig. 12(c). Finally, the nitrogen profile exhibits marginal enrichment of this element at the layer interfaces, which

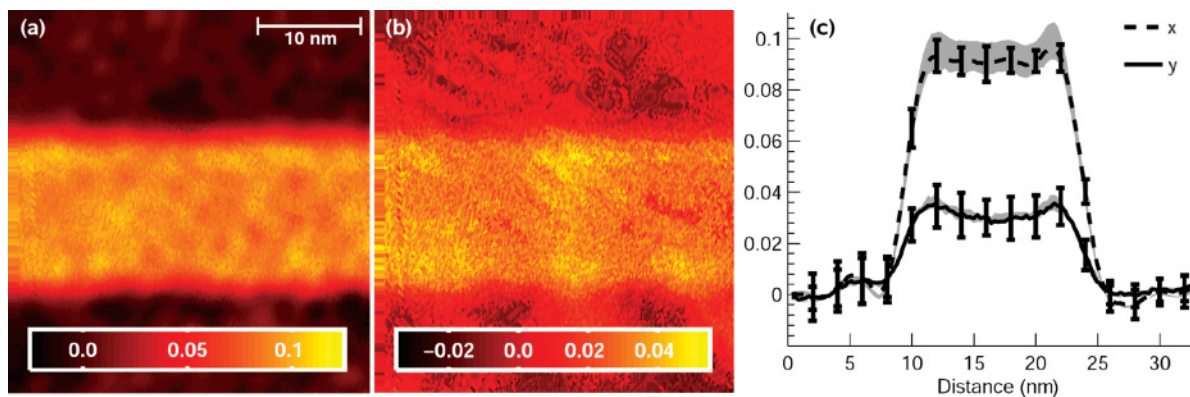


FIG. 12. (Color online) Concentration evaluation yielding (a) local indium and (b) local nitrogen distribution for sample II exemplarily for a thickness of 30 nm. (c) Respective profiles obtained by averaging horizontally in (a) and (b). Error bars are drawn each 2 nm only and indicate statistical fluctuations, and the gray corridor is a measure of error due to inaccurate knowledge of the specimen thickness. Three-beam images had been taken in zone axis [001] with the Laue circle center at (4.2 0 0).

nevertheless ranges inside the error bars. Whether this is indeed a physical effect or an artifact of, e.g., the measurement of local fringe distances, will be discussed in Sec. VI.

## VI. DISCUSSION

### A. Disorder in the Bloch-wave limit

By definition of additional absorptive form factors in Sec. IV A, we intended to close the gap between the correct simulation of Pendellösung plots under the influence of Huang scattering losses caused by SAD. Although not perfect, our approach agrees much better with a full multislice calculation than using absorptive form factors for thermal diffuse scattering alone. This is a marginal effect when only a few strong beams are excited, as is the case for the systematic row condition.<sup>15</sup> However, the method presented here relies on images taken near zone axis [001] where many beams are involved and the beam of interest, 020, is of low intensity. For example, neglect of Huang scattering decreases maximum concentrations in Fig. 9(c) by about 0.02 for indium and 0.01 for nitrogen.

A legitimate question is why the Bloch-wave approach is frequently used even in the presence of static besides thermal disorder, whereas multislice methods in combination with today's computer capacity can do without any symmetry requirements. Until now, this is true as long as chemical bonding is negligible, because the MASA approach yields bonding effects only for perfect crystals, or, equivalently, discrete spatial frequencies. Efficient full density functional theory calculations of the electron density in realistic crystal supercells are still too computationally demanding. Therefore, adapting the real part of the ideal crystal potential to bonding and SAD, and the imaginary part to losses arising from thermal and static disorder, means an efficient way to simulate diffraction patterns if only Bragg spots are of interest.

### B. Composition mapping

The three-beam method presented here is, in principle, a consequent combination of strain state analysis and composition evaluation by lattice fringe analysis (CELFA)<sup>18</sup> and requires low experimental effort provided that an aperture is available that suppresses nonlinear imaging artifacts on the 220 and 020 diffractogram reflections. In contrast to off-axis techniques,<sup>14,15,18,30</sup> the error of inaccurately known specimen thickness becomes significant, so indication of concentration-dependent corridors that contain solutions for physically plausible thicknesses should be part of final concentration profiles. Nevertheless, one should keep in mind that, even though the corridor in Fig. 9(c) corresponds to a thickness interval of 70 nm, errors for nitrogen are negligible and those for indium do not exceed  $\pm 0.01$ . However, comparison of Figs. 9 and 10 clearly shows that qualitative observations as to the correlation of indium and nitrogen distributions or shape of the layer are not influenced by this error.

In methodological respect, introduction of a new approach should meet two criteria: First, compared to previously reported techniques, application to the same samples must reproduce former reliable results. Second, it should extend applicability of existing TEM methods.<sup>14,15,31</sup> Concerning the

first argument, it was verified in Sec. V C that mean indium and nitrogen contents agree well with independently found results: For sample II, two-beam imaging under systematic row conditions yielded<sup>15</sup>  $\bar{x} = 0.08 \pm 0.01$ ,  $\bar{y} = 0.03 \pm 0.005$  for the mean concentrations. Additionally, band-gap measurements and x-ray diffraction applied to a sample grown under the same conditions confirmed this composition.<sup>3</sup> As to different TEM composition quantification techniques, three main arguments are worth mentioning: First, our approach is standardless in the sense that no ternary quantum well is needed as a reference, as is the case in the studies of Litvinov *et al.*<sup>31</sup> We can drop the assumption that indium incorporation during growth does not depend on that of nitrogen. Second, the present method is no longer limited to concentrations far from the phase jump, or, equivalently, to the significant presence of 020 fringes. This extends single-image compositional analysis to the important field of InGaNA<sub>s</sub> laser structures. Third, it becomes obvious from Sec. V A that an analysis of composition fluctuations relies on knowledge of both strain and chemical contrast for each lattice point that can hardly be assured by superposition of a systematic row dark field and a zone-axis high-resolution TEM image.<sup>14,30</sup> Of course, this procedure is less critical for InGaNA<sub>s</sub> layers having homogeneous composition laterally. However, a three-beam approach has been proposed already to solve this problem.<sup>14,15</sup>

### C. Annealing effects

Investigation of compositional fluctuations by TEM must critically be analyzed with respect to specimen thickness, because measured quantities are a superposition of sample properties in the zone-axis direction. Nevertheless, it is obvious that the island observed in Fig. 10 is indeed the image of a single island. If the specimen was much thicker than the mean distance between islands, being 20–30 nm according to Fig. 7, a blurred layer with homogeneous thickness would be observed. If so, the observation of an InGaNA<sub>s</sub> layer with homogeneous thickness after annealing in Fig. 9 could be due to this effect. However, the 020 fringe intensity would not vanish at the upper interface because at some specimen depth an area with pure GaAs would exist that violates the continuity condition for the transition between the two possible solutions according to Fig. 6. For thick regions of the as-grown sample Ib this effect was indeed observed.

In short, it is observed here that annealing changes long-range order of both indium and nitrogen. This results in a homogenization of the nitrogen distribution and symmetric indium concentration profiles. In particular, thermal annealing causes a dissolution of islands, which leads to a nearly homogeneously thick InGaNA<sub>s</sub> layer. This observation suggests that the increase of PL intensity by a factor of 20 and the spectral shift of about 60 meV to higher energies is due to a long-range homogenization of stoichiometry in our case. From the experimental point of view, the presence of nitrogen fluctuations in as-grown InGaNA<sub>s</sub> is controversially discussed in the literature. For example, Albrecht *et al.*<sup>11</sup> found indium fluctuations of  $\pm 0.05$  on length scales of 20 nm but homogeneous nitrogen content. In contrast, Herrera *et al.*<sup>32</sup> additionally report on nitrogen modulations, resulting in uncoupled indium-rich and nitrogen-rich regions. Common to

these analyses is the underlying dark-field imaging technique using, e.g., the 220 reflection. In this respect, simultaneous evaluation of both strain- and chemical-sensitive contrast at identical specimen positions is a requirement to clarify this issue. Thus, our results tend to confirm findings of Herrera *et al.*,<sup>32</sup> who interpret composition modulations and decoupling of nitrogen and indium profiles in the framework of spinodal decomposition. However, it is important to note that characteristics of the InGaNA<sub>s</sub> layer are highly dependent on growth conditions that differ among research groups.

Our PL spectra exhibit characteristic annealing behavior, since a blue shift of about 60 meV has also been found by Klar *et al.*<sup>4</sup> for the same annealing temperature. However, Klar *et al.* found no evidence for compositional fluctuations, even in the as-grown sample. Consequently, this group interprets annealing effects in terms of preferential coordination of nearest neighbors, that is, an affinity to form In-N bonds instead of Ga-N bonds, as has frequently been reported in conjunction with thermal annealing.<sup>4,8,12,30,33,34</sup> In this work, direct observation of the dissolution of compositional modulations during thermal annealing implies that the change in PL is due to homogenization of stoichiometry. Since Klar *et al.* used MOVPE, whereas sample I in this work was grown by MBE, one tends to assign different annealing mechanisms to both epitaxial techniques. In fact, there is no contradiction between both explanations, because annealing might also have caused preferential nearest-neighbor configurations here. In this respect, Figs. 10 and 9 imply that a dissolution of nitrogen- and indium-rich regions in favor of a more homogeneous layer ought to be accompanied by an increase of the frequency of In-N bonds.

In the strict sense, structure factors for random alloys, which determine all simulations in this work, should be modified to take into account preferential bond configurations. So far, we consider the effect on composition maps to be small with respect to experimental errors and point out that observations of long-range structural changes remain unchanged. Furthermore, both high-resolution and dark-field TEM provide only indirect access to study preferential nearest-neighbor configurations. Instead, it is advisable to make combined use of TEM and, e.g., extended x-ray-absorption fine-structure investigations, which are not available for the samples investigated here but left as a future task.

Additionally, literature offers various findings for the impact of annealing on the nitrogen profile. Grillo *et al.*<sup>14</sup> deduce strong nitrogen enrichment at the well edges, confirmed by later studies of Albrecht *et al.*<sup>30</sup> with the same method, where additional out-diffusion is found and assigned to the blue shift of PL peaks. In contrast, Volz *et al.* observed no annealing effect on nitrogen profiles in InGaNA<sub>s</sub>.<sup>10</sup> One common result of these groups and the present report is that annealing leads to lateral homogenization of nitrogen content, although the profiles themselves differ a lot. According to Fig. 9(c), a tendency of nitrogen to diffuse out of the well in the growth direction may be derived from the fact that both profiles are not centered around the same position, but this must be considered a minor effect, which is not responsible for the change in PL. Concerning the indium concentration profile, the Gaussian shape observed here after annealing, in principle, agrees with that of previous reports.<sup>30</sup>

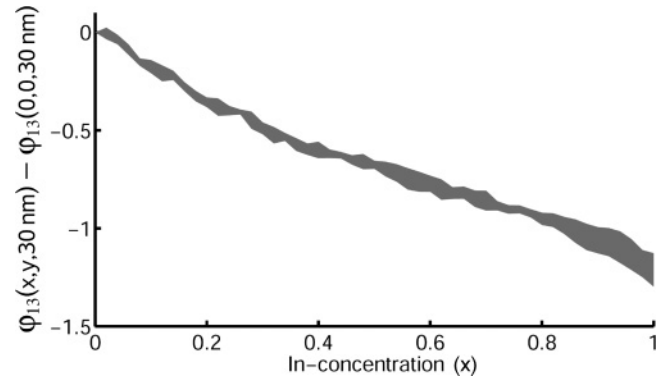


FIG. 13. Simulation of the 220 fringe phase dependence on In content  $x$  and nitrogen content  $y$  (gray corridor) according to Eq. (1). A constant specimen thickness of 30 nm was assumed. The influence of  $\varphi_{13}$  on composition measurement at interfaces is estimated in the text.

We finally pick up the evaluation of the local fringe distances at interfaces. Equation (1) contains a phase  $\varphi_{nm}$  that determines the position of the intensity maxima in addition to the local lattice constant and aberrations. This phase is constant only in the absence of composition gradients, which in turn means that composition gradients may simulate strain where is none. This chemical shift depends on compositions  $x$  and  $y$ , thickness, and magnitude of the gradient, which makes a comprehensive study difficult. Nonetheless, to get an impression of the consequences for the measurement of the normalized fringe distance, we exemplarily estimate the influence of this chemical shift on composition quantification for a specimen thickness of 30 nm. For the whole indium-concentration range, Fig. 13 depicts the dependence of  $\varphi_{13}$  on  $x$ , whereas the gray corridor represents the dependence on nitrogen content  $y \in [0 \dots 0.05]$ . Obviously  $\varphi_{13}$  is dominated by the dependence on  $x$ , which is almost linear. From that we can roughly estimate the error for measured compositions as follows. For a fictitious sharp interface between GaAs and InAs,  $\varphi_{13}$  changes about 1.5 rad, which makes the 220 fringe at the interface appear at a position that is shifted by about 25% of the native 220 fringe distance. Since the interface is sharp, this corresponds to an indium concentration gradient of about 2.5/nm. In contrast, present composition profiles exhibit gradients of less than  $0.3/(5 \text{ nm}) = 0.06/\text{nm}$ . Consequently, as  $\varphi_{13}$  proceeds linearly, we expect the real chemical shift to be only  $0.06/2.5 = 0.024$  of that for a sharp GaAs-InAs interface. In terms of strain state analysis based on the detection of 220 fringe positions, the present gradient causes the fringes to be displaced by 1.2 pm from the position determined solely by the geometric phase. By comparison of the resulting (erroneous) normalized fringe distance  $\varepsilon_{[010]}$  with Fig. 6, this can cause nitrogen content to be wrong by  $\Delta y \approx \pm 0.015$ . This error is expected to be present in many profiles; for example, nitrogen enrichment at well edges in Fig. 12(c) or negative nitrogen contents in Fig. 9(c) might be attributed to this artifact. Note that this effect is observed only in the presence of composition gradients and should especially be taken into account when comparing with the work of Albrecht *et al.*<sup>11,30</sup> and Grillo *et al.*,<sup>14</sup> where M-shaped nitrogen profiles have been found in InGaNA<sub>s</sub> quantum wells.

## VII. SUMMARY AND CONCLUSIONS

A method for the measurement of strain and contrast in quaternary InGaNAs was introduced, which allows for simultaneous quantification of indium and nitrogen content. The technique exploits one high-resolution TEM micrograph formed by three beams that are not coupled with respect to nonlinear imaging. Bloch-wave simulations of reference beam amplitudes included the finding of optimized imaging conditions and account for absorption ascribed to Huang scattering at SAD, as well as chemical bonding and the influence of SAD (found by VFF relaxation) on structure factors. Application of the three-beam method to an  $\text{In}_{0.28}\text{Ga}_{0.72}\text{N}_{0.025}\text{As}_{0.975}$  quantum layer before and after thermal annealing has shown that annealing caused a dissolution of indium- and nitrogen-rich regions in favor of a homogeneous layer with Gaussian-shaped indium profile. In addition, recorded room-temperature photoluminescence exhibits a blue shift of about 60 meV and an increase by a factor of 20 after annealing, for which the observed structural changes were made responsible.

In this contribution, method and application take equal part so the latter was restricted to one as-grown and one annealed structure. From the significant redistribution of impurity atoms of all species on length scales of 10 nm we conclude that interpretation of PL spectra solely in the context of nearest-neighbor configurations can be insufficient. However,

detailed understanding of structural transitions as a function of annealing conditions such as temperature or pressure and correlation to optical properties and growth conditions is left as a future task.

As our method falls in the category of conventional high-resolution TEM without the explicit need for advanced equipment such as imaging correctors, it is easy to apply, provided that a proper objective aperture for three-beam imaging is available. In principle, the same holds for the simulation of reference data since Bloch-wave simulations are capable for desktop computers. This holds even if bonding and SAD are to be included since MASA and VFF provide efficient but accurate approximations, respectively. In that respect absorptive form factors for SAD scattering derived here are not only of academic interest but may also affect concentration profiles more or less strongly, depending on the amount of nitrogen and imaging conditions.

## ACKNOWLEDGMENTS

This work was supported by the Deutsche Forschungsgemeinschaft (DFG) under contract nos. RO 2057/4, SCHO 1196/3, VO805/4, and VO805/5. K.M. also thanks the Physics International Postgraduate Programme (PIP) at Bremen University.

\*mueller@ifp.uni-bremen.de

- <sup>1</sup>M. Kondow, T. Kitatani, M. C. Larson, K. Nakahara, K. Uomi, and H. Inoue, *J. Cryst. Growth* **188**, 255 (1998).
- <sup>2</sup>M. Hetterich, M. D. Dawson, A. Y. Egorov, D. Bernklau, and H. Riechert, *Appl. Phys. Lett.* **76**, 1030 (2000).
- <sup>3</sup>K. Volz, W. Stolz, J. Teubert, P. J. Klar, W. Heimbrodt, F. Dimroth, C. Baur, and A. W. Bett, in *Dilute III/V Nitride Semiconductors and Material Systems* (Springer, Berlin, 2008), pp. 369–404.
- <sup>4</sup>P. J. Klar, H. Grüning, J. Koch, S. Schäfer, K. Volz, W. Stolz, W. Heimbrodt, A. M. Kamal Saadi, A. Lindsay, and E. P. O'Reilly, *Phys. Rev. B* **64**, 121203 (2001).
- <sup>5</sup>H. Djie, D.-N. Wang, B. Ooi, J. Hwang, X.-M. Fang, Y. Wu, J. Fastenau, and W. Liu, *Thin Solid Films* **515**, 4344 (2007).
- <sup>6</sup>J.-Y. Duboz, J. A. Gupta, Z. R. Wasilewski, J. Ramsey, R. L. Williams, G. C. Aers, B. J. Riel, and G. I. Sproule, *Phys. Rev. B* **66**, 085313 (2002).
- <sup>7</sup>A. Pomarico, M. Lomascolo, R. Cingolani, A. Y. Egorov, and H. Riechert, *Semicond. Sci. Technol.* **17**, 145 (2002).
- <sup>8</sup>O. Rubel, K. Volz, T. Torunski, S. D. Baranovskii, F. Grosse, and W. Stolz, *Appl. Phys. Lett.* **85**, 5908 (2004).
- <sup>9</sup>K. Kim and A. Zunger, *Phys. Rev. Lett.* **86**, 2609 (2001).
- <sup>10</sup>K. Volz, T. Torunski, O. Rubel, W. Stolz, P. Kruse, D. Gerthsen, M. Schowalter, and A. Rosenauer, *J. Appl. Phys.* **102**, 083504 (2007).
- <sup>11</sup>M. Albrecht, V. Grillo, T. Remmele, H. P. Strunk, A. Y. Egorov, G. Dumitras, H. Riechert, A. Kaschner, R. Heitz, and A. Hoffmann, *Appl. Phys. Lett.* **81**, 2719 (2002).
- <sup>12</sup>K. Volz, T. Torunski, O. Rubel, and W. Stolz, *J. Appl. Phys.* **104**, 053504 (2008).

- <sup>13</sup>C. S. Peng, E. M. Pavelescu, T. Jouhti, J. Konttinen, and M. Pessa, *Solid-State Electron.* **47**, 431 (2003).
- <sup>14</sup>V. Grillo, M. Albrecht, T. Remmele, H. P. Strunk, A. Yu. Egorov, and H. Riechert, *J. Appl. Phys.* **90**, 3792 (2001).
- <sup>15</sup>K. Müller, M. Schowalter, A. Rosenauer, O. Rubel, and K. Volz, *Phys. Rev. B* **81**, 075315 (2010).
- <sup>16</sup>P. N. Keating, *Phys. Rev.* **145**, 637 (1966).
- <sup>17</sup>A. Rosenauer, M. Schowalter, F. Glas, and D. Lamoen, *Phys. Rev. B* **72**, 085326 (2005).
- <sup>18</sup>A. Rosenauer, U. Fischer, D. Gerthsen, and A. Förster, *Ultramicroscopy* **72**, 121 (1998).
- <sup>19</sup>A. Rosenauer and M. Schowalter, in *Springer Proceedings in Physics*, edited by A. G. Cullis and P. A. Midgley, (Springer, Berlin, 2007), Vol. 120, pp. 169–172.
- <sup>20</sup>M. Schowalter, A. Rosenauer, J. T. Titantah, and D. Lamoen, *Acta Crystallogr. Sect. A* **65**, 5 (2009).
- <sup>21</sup>A. Rosenauer, M. Schowalter, J. T. Titantah, and D. Lamoen, *Ultramicroscopy* **108**, 1504 (2008).
- <sup>22</sup>A. Weickenmeier and H. Kohl, *Acta Crystallogr. Sect. A* **47**, 590 (1991).
- <sup>23</sup>D. M. Bird and Q. A. King, *Acta Crystallogr. Sect. A* **46**, 202 (1990).
- <sup>24</sup>O. Rubel, I. Németh, W. Stolz, and K. Volz, *Phys. Rev. B* **78**, 075207 (2008).
- <sup>25</sup>F. Glas, *Philos. Mag.* **84**, 2055 (2004).
- <sup>26</sup>D. Van Dyck, *Ultramicroscopy* **109**, 677 (2009).
- <sup>27</sup>K. Huang, *Proc. R. Soc. London A* **190**, 102 (1947).
- <sup>28</sup>C. R. Hall, P. B. Hirsch, and G. R. Booker, *Philos. Mag.* **14**, 979 (1966).

- <sup>29</sup>Z. L. Wang, *Elastic and Inelastic Scattering in Electron Diffraction and Imaging* (Plenum Press, New York, 1995).
- <sup>30</sup>M. Albrecht, H. Abu-Farsakh, T. Remmele, I. Hausler, L. Geelhaar, H. Riechert, and J. Neugebauer, *Phys. Rev. Lett.* **99**, 206103 (2007).
- <sup>31</sup>D. Litvinov, D. Gerthsen, A. Rosenauer, M. Hetterich, A. Grau, P. Gilet, and L. Grenouillet, *Appl. Phys. Lett.* **85**, 3743 (2004).
- <sup>32</sup>M. Herrera, D. Gonzalez, M. Hopkinson, M. Gutierrez, P. Navaretti, H. Y. Liu, and R. Garcia, *J. Appl. Phys.* **97**, 073705 (2005).
- <sup>33</sup>O. Rubel, B. Kunert, S. D. Baranovskii, F. Grosse, K. Volz, and W. Stolz, *Phys. Rev. B* **74**, 195206 (2006).
- <sup>34</sup>A. Jenichen, C. Engler, G. Leibiger, and V. Gottschalch, *Surf. Sci.* **574**, 144 (2005).